

Implementation and Applications of the Hydrodynamic Model in a General Purpose Device Simulator

V. Axelrad*, G. Rollins, S. Motzny, M. Jaczynski
Technology Modeling Associates, Palo Alto, California, USA

Abstract

Local carrier heating and nonstationary effects in deep-submicron silicon devices can lead to substantial deviation between simulation results of classical device simulators and experimental data. A significant improvement of the physical accuracy of the simulation is achieved by adding a self-consistent solution of the carrier energy balance equation to the classical drift-diffusion set of equations. A description of the implementation of the hydrodynamic model is given along with two application examples — a submicron MOSFET and a BJT.

1 Introduction

Numerical modeling of advanced deep-submicron semiconductor devices requires a revision of the classically used numerical models. In very small devices, the mobile carriers can no longer be assumed to be in thermal equilibrium with the lattice. In regions of high electric field, carrier mean energy can be substantially higher than the thermal energy associated with the lattice temperature, assumed by the classical drift-diffusion equations [1]. Local carrier heating introduces a variety of effects in the device, ranging from thermal diffusion contributing to the total current density to velocity saturation effects or, more accurately, carrier energy-dependent mobility. Physically accurate treatment of local carrier heating (and cooling) effects is generally expected to improve the predictive capabilities of simulation for small devices, where hot-carrier effects are increasingly important.

The improved physical accuracy of the model is demonstrated by the application examples presented in this paper. The results show significant differences between the classical drift-diffusion model and the hydrodynamic model. Carrier heating is substantial in both magnitude and affected area of the devices presented, demonstrating the inadequacy of the thermal equilibrium assumptions for these types of submicron devices.

The following is a discussion of the self-consistent solution of the Poisson's, current continuity, and carrier energy balance equations based on the general purpose device simulator TMA PISCES-2B¹. The new model has been successfully tested for various devices including ballistic diodes, BJTs, bulk MOSFETs and SOI-MOSFETs. The implemented set of equations, discretization strategy and convergence properties are presented.

*Permanent address: Chair for Integrated Circuits, Technical University Munich, Germany

¹TMA PISCES-2BTM is a trademark of Technology Modeling Associates, Inc., Palo Alto, California, USA.

2 The Hydrodynamic Model

The implemented hydrodynamic model includes the classical drift-diffusion set of equations for the electric potential and carrier concentrations as implemented in PISCES [2, 3]:

$$\nabla \cdot \epsilon \nabla \psi = -q(p - n + N_D^+ - N_A^-) - \rho_F \quad (1)$$

$$\frac{1}{q} \nabla \cdot \vec{J}_n = +U_n + \frac{\partial n}{\partial t} \quad (2)$$

$$\frac{1}{q} \nabla \cdot \vec{J}_p = -U_p - \frac{\partial p}{\partial t} \quad (3)$$

Local carrier heating or cooling results in an additional thermal diffusion term in the generalized expression for the electron current density (the standard drift-diffusion expression is used for the hole current density \vec{J}_p):

$$\vec{J}_n = -q\mu_n [n\vec{E} + \nabla(u^T n)] \quad (4)$$

The carrier thermal voltage $u^T = kT/q$ is determined by the energy balance equation [4, 5]:

$$\nabla \cdot \vec{S}_n = \frac{1}{q} \vec{J}_n \cdot \vec{E} - \frac{3}{2} \left\{ n \frac{u^T - u^{T_0}}{\tau_w} + \frac{\partial(nu^T)}{\partial t} \right\} \quad (5)$$

$$\vec{S}_n = -\frac{5}{2} u^T \left[\frac{\vec{J}_n}{q} + c_q \mu_n n \nabla u^T \right] \quad (6)$$

The energy relaxation time τ_w has been chosen to be 0.4ps as in [4, 6]. A carrier temperature-dependent mobility model based on the one suggested in [5] has been implemented, enabling a description of the velocity overshoot effect (v_s denotes the saturation velocity):

$$\mu_n(u^T) = \mu_0 \left\{ 1 + [\alpha(u^T - u^{T_0})]^\beta \right\}^{-1/\beta} \quad (7)$$

$$\alpha = \frac{3\mu_0}{2v_s^2 \tau_w}, \quad \beta = 2$$

The low-field mobility μ_0 can be chosen from the variety of models implemented in TMA PISCES-2B [3], such as doping-dependent, carrier concentration-dependent, surface mobility models, etc.

3 Discretization

3.1 Box Integration

Following the discretization procedure implemented in PISCES [2, 3], a box integration procedure is applied on a triangular grid. All equations of the hydrodynamic model — Poisson's equation, current continuity equations and the energy balance equation — are of the form $\nabla \cdot \vec{F} = R$.

The divergence operators are transformed to integral form using the Gauss theorem around the node number i with the boundary l and the enclosed area A :

$$\oint_l \vec{F} \cdot d\vec{l} = \iint_A R dA \quad (8)$$

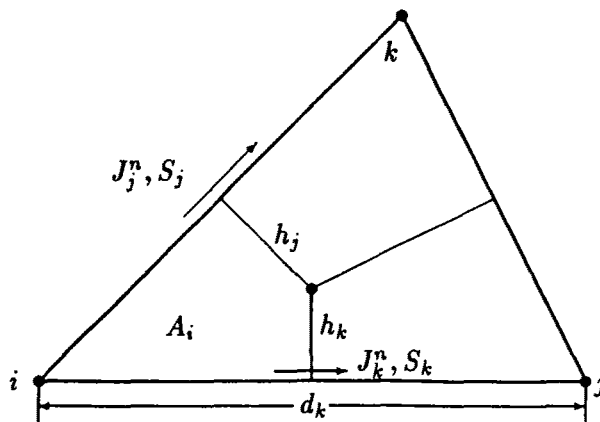


Figure 1: Box Integration — method of perpendicular bisectors.

Using the notation of Fig. 1, the discrete form of eq. (8) reads (summation over all triangles surrounding the node i):

$$\sum_{m=1}^M [h_{j_m} F_{j_m} + h_{k_m} F_{k_m} - A_{i_m} R_{i_m}] = 0 \quad (9)$$

3.2 Current Continuity Equations

The discretization of the current continuity equation follows the classical Scharfetter-Gummel approach [7]. The electron current density in 1D reads (primes denote spatial derivatives):

$$J_n = -q\mu_n \left[\{E + (u^T)'\} n + u^T n' \right] \quad (10)$$

Standard assumptions required for an analytic integration of eq. (10) in the interval between adjacent grid nodes are maintained:

$$\frac{J_n}{\mu_n} = \text{const}, \quad E = \text{const}, \quad u^T = \text{const} \quad (11)$$

To integrate eq. (10) we add a new assumption of constant effective electric field $E_{eff} = E + (u^T)'$, i.e. $(u^T)' = \text{const}$. This is consistent with the physical meaning of the assumptions in eq. (11): constant driving force of the drift current and constant diffusion coefficient $D_n = \mu_n \bar{u}^T$, where \bar{u}^T is an average thermal voltage. The latter appears to be a reasonable approximation.

Using these assumptions we obtain the following expression for the current density along the side k connecting nodes (i, j) of a triangle Fig. 1 ($B(\cdot)$ denotes the Bernoulli function):

$$J_k^n = \frac{\mu_k}{d_k} \bar{u}_k^T [n_j B(\Delta_k) - n_i B(-\Delta_k)] \quad (12)$$

$$\Delta_k = \frac{\psi_j - \psi_i - u_j^T + u_i^T}{\bar{u}_k^T}, \quad \bar{u}_k^T = \frac{u_i^T + u_j^T}{2}$$

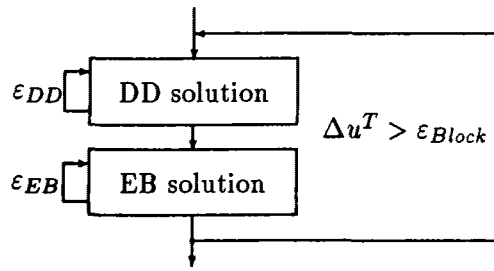


Figure 2: Solution strategy.

3.3 Energy Balance Equation

Two steps are important in the discretization of the energy balance equation eq. (5):

- i) discrete representation of the energy flow \vec{S}_n ,
- ii) discretization of the heating term $\vec{J}_n \cdot \vec{E}$.

The energy flow along the side (i, j) in the element (cf. Fig. 1) is represented by:

$$S_k = -\frac{5}{2} \bar{u}^T \left[\frac{J_k^n}{q} + c_q \mu_k^n \bar{n} \frac{u_j^T - u_i^T}{d_k} \right] \quad (13)$$

$$\bar{n} = \frac{1}{d_k} \int_{x_i}^{x_j} n(x) dx = n_i + (n_j - n_i) \cdot \left(\frac{1}{1 - \epsilon \Delta_k} + \frac{1}{\Delta_k} \right)$$

The heating term $\vec{J}_n \cdot \vec{E}$ is integrated over the entire triangular element. The contribution H_i to the node i from the heat generated in the triangle (i, j, k) is (cf. Fig. 1):

$$H_i = A_i (E_x J_{x,av}^n + E_y J_{y,av}^n) \quad (14)$$

where $J_{x,av}^n, J_{y,av}^n$ are average values of the current density in the element.

4 Decoupled Solution

A decoupled approach (Fig. 2) has been chosen for the self-consistent solution of the hydrodynamic model. The algorithm consists of a solution of the drift-diffusion eqs. (1-4) for the classical variables ψ, n, p , followed by a solution of the energy balance equation (5) for the electron thermal voltage u^T . The new temperature distribution is used to re-evaluate ψ, n, p . This procedure is repeated until updates of the temperature Δu^T fall below a limit ϵ_{Block} specified by the user. In case of non-convergence of either the drift-diffusion solution or energy balance solution the applied bias voltage is reduced and the solution process is repeated.

The convergence of the block iteration Fig. 2 is generally fast. The convergence rate typically slows down at high current levels; it also depends on the type of device under investigation. Problems are observed at low current densities and for irregular or coarse grids. These problems appear to be related to insufficient accuracy of the current density.

The convergence behavior is illustrated by Fig. 3, showing the magnitude of the temperature updates during the simulation of a bipolar transistor (cf. application examples).

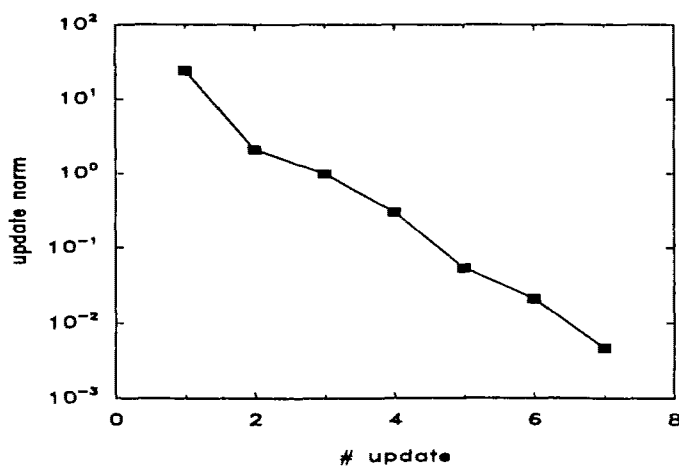


Figure 3: Scaled temperature updates $T/T_0, T_0 = 300K$ during the simulation of a BJT.

5 Applications

An N-type submicron LDD MOSFET with an effective channel length of $0.3\mu\text{m}$ serves as the first test device to demonstrate the new hydrodynamic model. Fig. 4 presents the mesh used for the simulation. The mesh has been obtained by regriding of the initial mesh based on temperature variation. The initial mesh originated from the process simulation of the structure with TSUPREM-4².

Fig. 5 presents the contour lines of the electron temperature in the NMOS calculated for bias conditions $V_S = 0V, V_G = 1.0V, V_D = 3.3V, V_{Sub} = 0$. Maximum carrier heating to about $4000K$ occurs near the corner of the drain-substrate junction. A mesh refinement has been performed to resolve the fast variation of the temperature in the hot reverse-biased drain-substrate junction.

Local carrier heating results in an additional thermal diffusion current in the hot area, significantly increasing the electron concentration in comparison to classical drift-diffusion models, as shown in Figs. 6, 7. The new model predicts a smoother electron distribution in the channel, higher electron concentration in the substrate and a significant spread of the electron concentration into the substrate.

The spread of the electron concentration results in a spread of the electron current density shown in Figs. 8, 9.

A second application example is an NPN bipolar junction transistor with a base width of $0.1\mu\text{m}$. The simulation grid is presented in Fig. 10. Convergence of the nonlinear block iteration for this device is presented in Fig. 3, which displays the norms of temperature updates after bias conditions $V_E = 0, V_B = 0.8V, V_C = 2.0V$ have been applied in one step. The total cpu-time was 15 minutes on a SparcStation 1+, whereas a drift-diffusion solution on the same grid requires 4 min.

Fig. 11 displays the electron temperature in the transistor along the vertical line $x = 0$. For comparison, scaled electric field distributions computed using the hydrodynamic (solid line) and the drift-diffusion model (dashed line) are also given. Electron temperature has a substantially different shape than the electric field. The maximum carrier energy is reached after the peak electric field. Since lower carrier energy results in higher mobility (eq. (7)), carrier mean velocity

²TSUPREM-4TM is a trademark of Technology Modeling Associates, Inc., Palo Alto, California, USA.

can significantly exceed the saturation velocity. This velocity overshoot effect is demonstrated in Fig. 12. Carrier mean velocity $\bar{v}_n = \bar{J}_n/(qn)$ exceeds the velocity saturation value 10^7 cm/s (dashed line, drift-diffusion solution) at the base-collector junction. These results qualitatively agree with the one-dimensional simulation in [6].

6 Conclusions

Availability of the carrier mean energy is expected to greatly improve the physical accuracy of numerical models of deep-submicrometer devices especially when hot-carrier effects are relevant. A practical implementation of the hydrodynamic set of equations has been carried out based on the widely used general purpose device simulator PISCES-2B. Applications of the new model to submicron devices disclose important effects previously not observable in simulation results.

References

- [1] W.V. v. Roosbroeck. Theory of flow of electrons and holes in germanium and other semiconductors. *Bell Syst. Techn. J.*, 29:560–607, 1950.
- [2] C.H. Price. *Two-Dimensional Numerical Simulation of Semiconductor Devices*. PhD thesis, Stanford University, Stanford, California, May 1982.
- [3] Technology Modeling Associates, Inc., Palo Alto, California, USA. *TMA PISCES-2B user's manual*, Nov 1990.
- [4] A. Forghieri, R. Guerreri, P. Ciampolini, A. Gnudi, M. Rudan, and G. Baccarani. A new discretization strategy of the semiconductor equations comprising momentum and energy balance. *IEEE Trans. on CAD*, 7(2), Feb. 1988.
- [5] B. Meinerzhagen and W.L. Engl. The influence of the thermal equilibrium approximation on the accuracy of classical two-dimensional numerical modeling of silicon submicrometer MOS transistors. *IEEE Trans. on Electron Devices*, 35(5):689–697, May 1988.
- [6] R.K. Cook. Numerical simulation of hot-carrier transport in silicon bipolar transistors. *IEEE Trans. on Electron Devices*, ED-30(9), Sept 1983.
- [7] D. Scharfetter and H.K. Gummel. Large signal analysis of a silicon read diode oscillator. *IEEE Trans. Electron Devices*, ED-16, 1969.

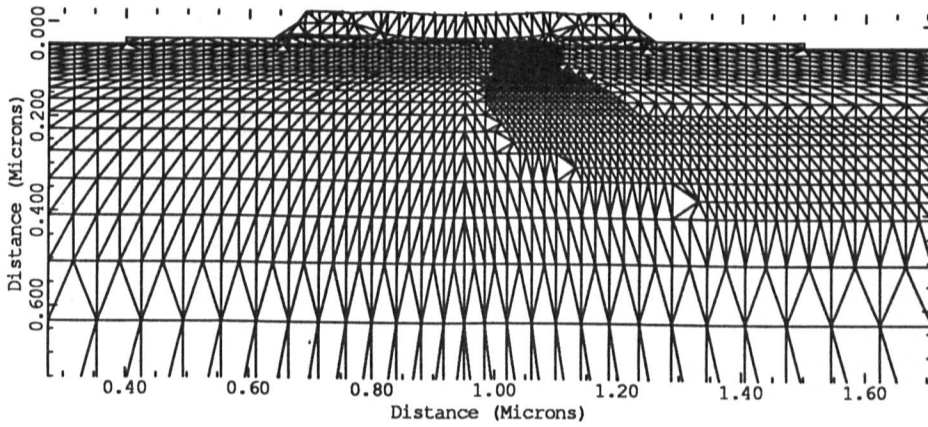


Figure 4: NMOS simulation grid (1696 nodes).

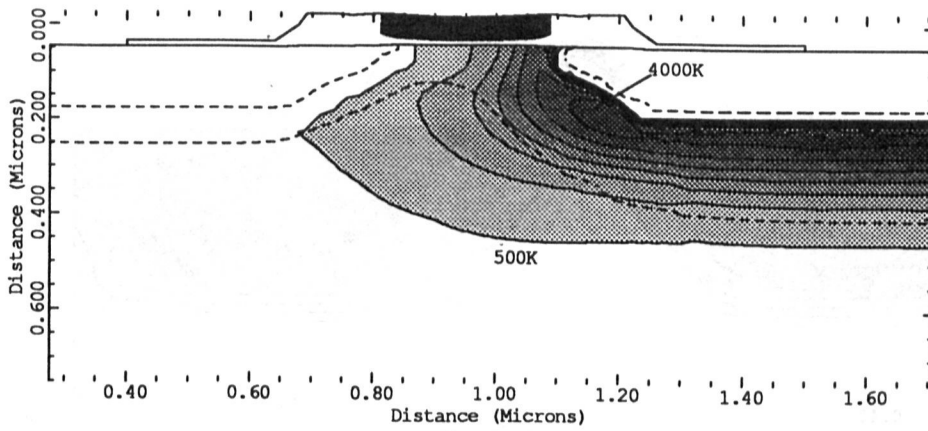


Figure 5: Electron temperature contour lines $T = 500K, 1000K, 1500K, \dots$. Dashed lines represent depletion zone edges.

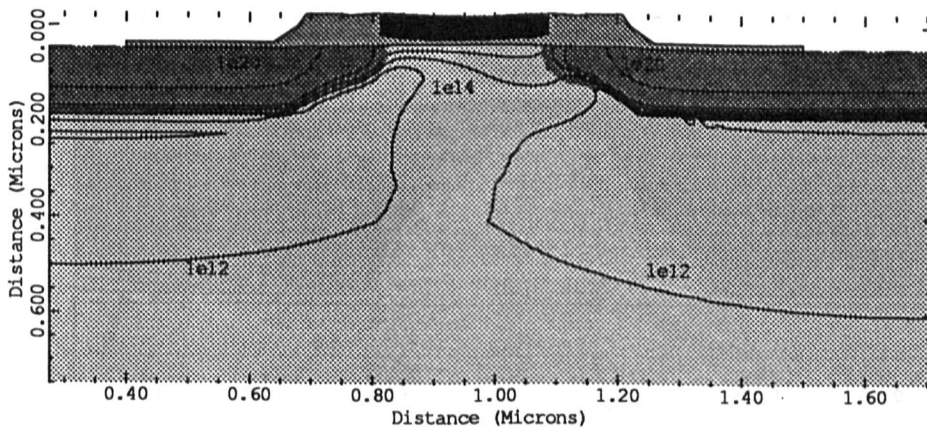


Figure 6: Electron concentration contour lines $n = 10^{20,18,16, \dots} \text{cm}^{-3}$ (hydrodynamic model).

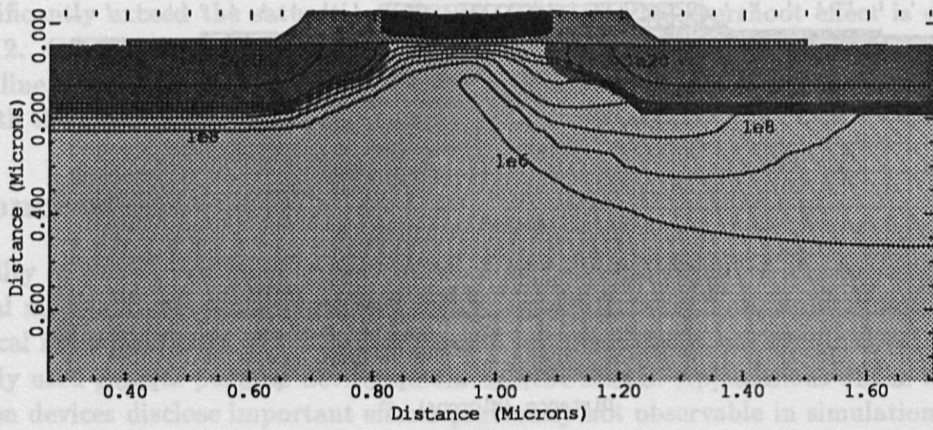


Figure 7: Electron concentration contour lines $n = 10^{20,18,16,\dots}\text{cm}^{-3}$ (drift-diffusion model).

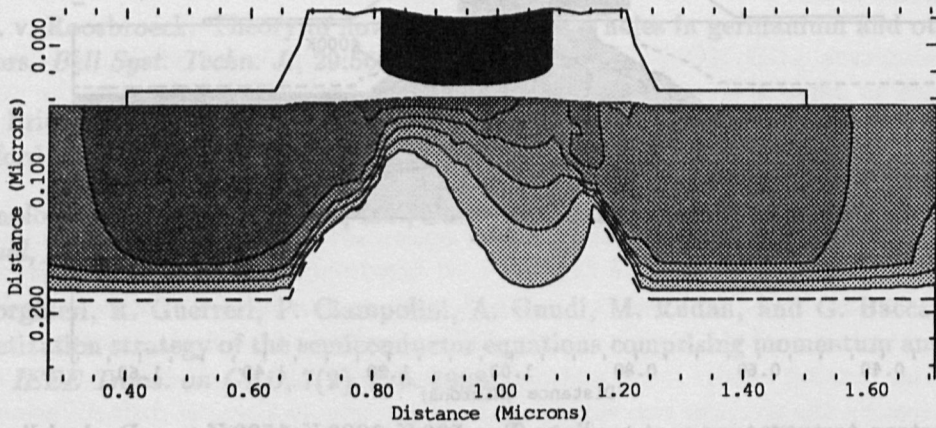


Figure 8: Electron current density contour lines (log scale) (hydrodynamic model).

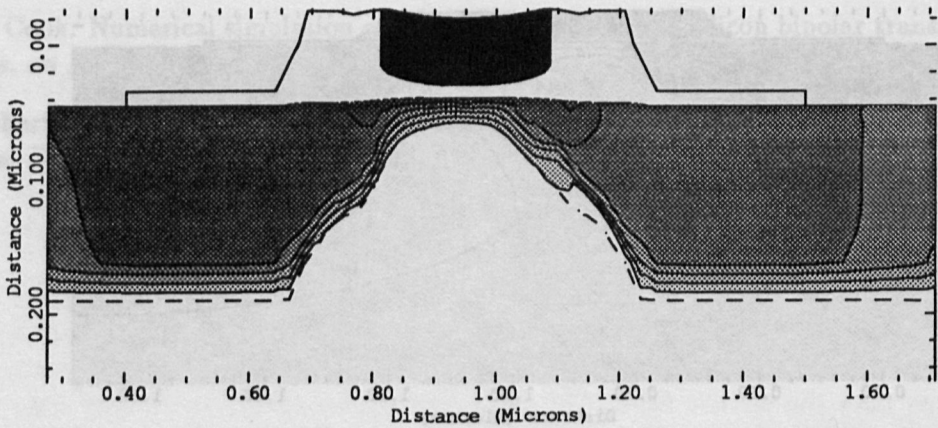


Figure 9: Electron current density contour lines (log scale) (drift-diffusion model).

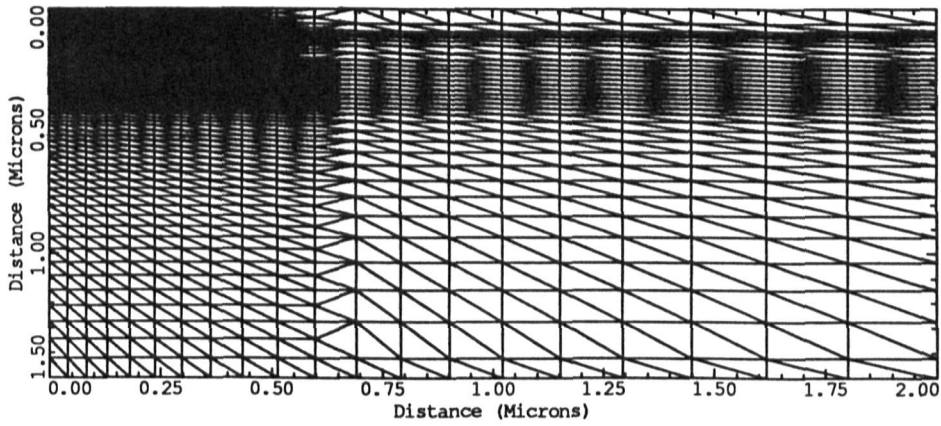


Figure 10: Bipolar transistor simulation grid (1306 nodes).

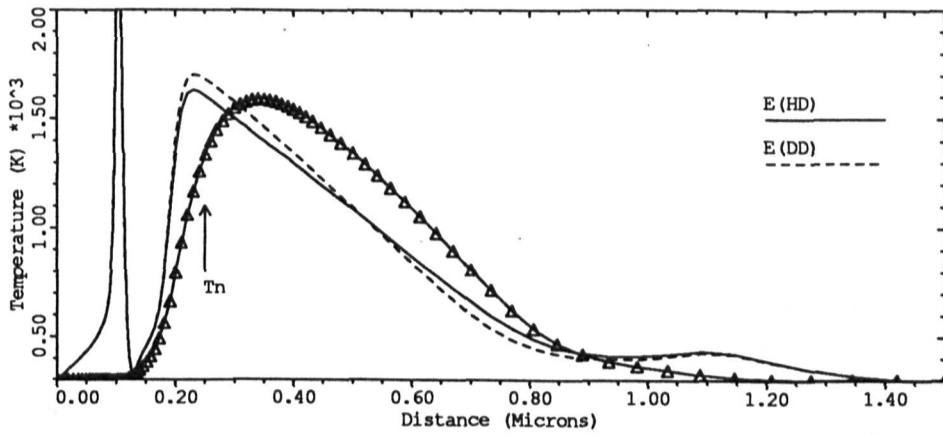


Figure 11: BJT carrier temperature (triangles) and electric field (scaled by $\frac{2v_g\tau_wq}{3k}$) along $x = 0$.

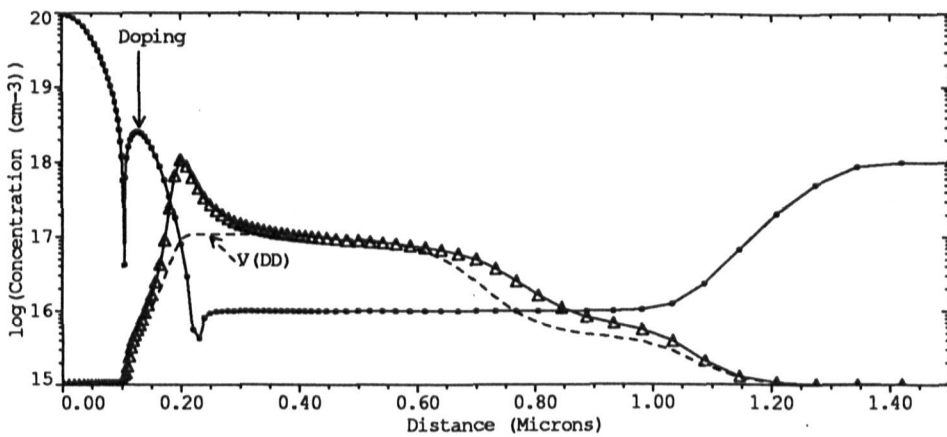


Figure 12: BJT doping concentration (circles) and electron mean velocity (hydrodynamic model — triangles; drift-diffusion — dashed line)